Activation mechanism of mitochondrial translation by LRPPRC-SLIRP

Vivek Singh[1], Yuzuru Itoh[1], Martijn A. Huynen[2], Alexey Amunts[1*]

[1] Science for Life Laboratory, Department of Biochemistry and Biophysics, Stockholm University, 17165 Solna, Sweden.
[2] Centre for Molecular and Biomolecular Informatics, Radboud Institute for Molecular Life Sciences, Radboud University Medical Center, Nijmegen, the Netherlands.

* correspondence: amunts@scilifelab.se

In mammalian mitochondria, mRNAs are co-transcriptionally stabilized by LRPPRC. Here we show that LRPPRC forms a stable complex with SLIRP and the mitoribosome to act as a carrier of genetic information, thus linking elements of the gene expression system. The structure of translating human mitoribosome in complex with LRPPRC-SLIRP shows how the mRNA is delivered for translation along a corridor formed by LRPPRC with proteins of the mitoribosomal small subunit mS31-mS39.

The mechanism of translation starts with a key step of binding mRNA that is delivered upon transcription by RNA polymerase (RNAP). In bacteria, physical transcription-translation coupling has been characterised[1-3]. However, in mammalian mitochondria, nucleoids are not compartmented with protein synthesis, and mitoribosomes are independently tethered to the membrane[4,5]. Thus, nascent mRNAs are thought to be protected from degradation by a large 130-kDa protein factor LRPPRC (leucine-rich pentatricopeptide repeat-containing protein), a member of the metazoa-specific protein kinase G tetratricopeptide repeat family. LRPPRC acts as an mRNA chaperone that binds co-transcriptionally, prevents secondary structure formation, and stabilizes mRNA structure by stimulating the activity of mitochondrial poly(A)polymerase[6-9]. Mutations in LRPPRC lead to a paediatric neurodegenerative disorder caused by damage in mitochondrial energy conversion that has no treatment[10]. LRPPRC has also been implicated in coordination of mitochondrial translation[6,11,12]. It has been further reported to interact with a small 11-kDa protein cofactor SLIRP (SRA stem-loop-interacting RNA-binding protein) that plays roles in LRPPRC stability and maintaining steady-state mRNA levels[13]. *SLIRP* silencing results in destabilization of respiratory complexes and loss of enzymatic activity, implicating a role in mRNA homeostasis[14], whereas *SLIRP* variants also cause a respiratory deficiency that leads to mitochondrial encephalomyopathy[15] In addition, *SLIRP* knockdown results in increased turnover of LRPPRC[13,15,16], and *in vivo* co-stabilisation has been shown[13,17], suggesting that the two entities might have interdependent functions. However, there are no structures available for LRPPRC, SLIRP or any complexes containing them, and thus although mitoribosomal models have been determined[18,19], the molecular mechanisms of mRNA binding and association with interacting partners remained unknown.

To explore the molecular basis for translation activation in human mitochondria, we used low salt conditions to isolate a mitoribosome:LRPPRC-SLIRP-mRNA complex for cryo-EM. We merged particles containing tRNAs in the A- and P-site as well as an extra density in the vicinity of the mRNA channel, and applied iterative masked focused refinement and classification with signal subtraction that resulted in a 2.9 Å resolution map of the mitoribosome:LRPPRC-SLIRP complex (3.4 Å local resolution) trapped during mRNA delivery to the mitoribosomal small subunit (SSU) (Extended Data Fig. 1). The reconstruction showed a clear density for the LRPPRC N-terminal domains bound to the mitoribosome, while the C-terminal domains were too flexible for modeling. It allowed us to model 34 α-helices, 9 of which form a superhelical ring-like architecture (head), while the rest form an extended tail that adopts a 90° curvature and outspreads 110 Å from the SSU body in parallel to the L7/L12 stalk (Fig. 1a,b). The LRPPRC head in our structure corresponds to the nuclear export signal (NES) domain, whereas the tail comprises the Epsin N-terminal homology (ENTH) domain (Fig. 1c). Upon completing of the LRPPRC building, the remaining associated density was assigned as SLIRP that is close to the LRPPRC tail. When LRPPRC-SLIRP is bound to the mitoribosome, a fragmented density of mS31 extending from the core also becomes ordered, revealing its N-terminal region. It is arranged in two helix-turn-helix motifs, offering a 1930 $Å^2$ surface area for direct interactions with LRPPRC. This singled out a density for mRNA, into which we modeled 42 residues,

numbered from the E-site codon. Thus, in the complete mitoribosome:LRPPRC-SLIRP-mRNA model, LRPPRC performs three functions: coordination of SLIRP, which plays a key role in the process of mRNA recruitment, association with the SSU, and handing-off the mRNA for translation (Fig. 1, Extended Data Fig. 2a-c, Supplementary Video 1).

The binding of SLIRP in our model is enabled via LRPPRC helices α20 and 22, which is consistent with crosslinking mass-spectrometry data[20]. The structure reveals that SLIRP links the head with the curved region of the LRPPRC tail that induces its specific shape (Fig. 1b). This binding of SLIRP coincides with the start of a corridor formed by mS31 and mS39 (Fig. 1b, Supplementary Video 1). Moreover, the SLIRP density is continuous with that of mRNA, which extends through the tunnel, and further over more than 180 Å through the SSU mRNA channel all the way to the decoding center. Thus, SLIRP contributes to the LRPPRC specific scaffold, and also accounts for a role in binding the mRNA. Our findings that SLIRP is involved in coupling to the mitoribosome provide a mechanistic explanation for results from biochemical studies showing that SLIRP affects LRPPRC properties *in vitro*[17,20], and the presentation of mRNA to the mitoribosome *in vivo*[13].

The association of LRPPRC with the mitoribosome involves the helices α1, 2, 4, 7-14 that form a mitoribosome-binding head (Fig. 1b,c). The binding is mediated by four distinct contacting regions (Fig 1c and Extended Data Fig. 5c): 1) α1-2 (residues 64-95) is flanked by a region of mS39, a PPR domain-containing protein, that consists of four bundled helices (α11-14); 2) α7 and 9 form a shared bundle with two N-terminal helices of mS31 (residues 175-208, stabilized by C-terminal region of mS39) that encircle the head to complement the PPR domain; 3) α10-12 are capped by a pronounced turn of mS31 (residues 209-232) acting as a lid that marks the LRPPRC boundary, and it is sandwiched by the mS39 helix α19 and C-terminus from the opposite side; 4) in addition, α11 is also positioned directly against the helix α23 of mS39. Thus, LRPPRC docks onto the surface of the mitoribosome via mS31-mS39, which are tightly associated with each other, and each provides two contact patches to contribute to stable binding.

The handing-off the mRNA for translation is mediated by four of the LRPPRC helical repeats: α1, 2, 16 and 18 (Fig. 1b,c, Supplementary Video 1). The mRNA nucleotides 33-35 are stabilized in a cleft formed by α1-2 from one side of the head and α16, 18 from the other. Nucleotides 31 and 32 are recognized by several arginine residues from the respective helices. The involvement of the NES-rich domain of LRPPRC in mRNA binding in our structure is consistent with a biochemical analysis of a recombinant protein where the N-terminal PPR segments were systematically removed, which showed a reduced formation of protein-RNA complexes[21]. The rest of the mRNA is situated too far to interact with LRPPRC. Here, the mRNA is handed to mS31-mS39, and the three proteins together form a 60-Å long corridor that channels the mRNA from SLIRP towards the mitoribosomal core (Fig. 1b, Supplementary Video 1). Nucleotides 26-30 run along with mS39 PPR domain 5, and nucleotide 26 connects to contact-2, where R219 of mS31 extends towards the base. Thus, the mRNA handing-off is achieved through a functional cooperation between LRPPRC-SLIRP and mS31-mS39.

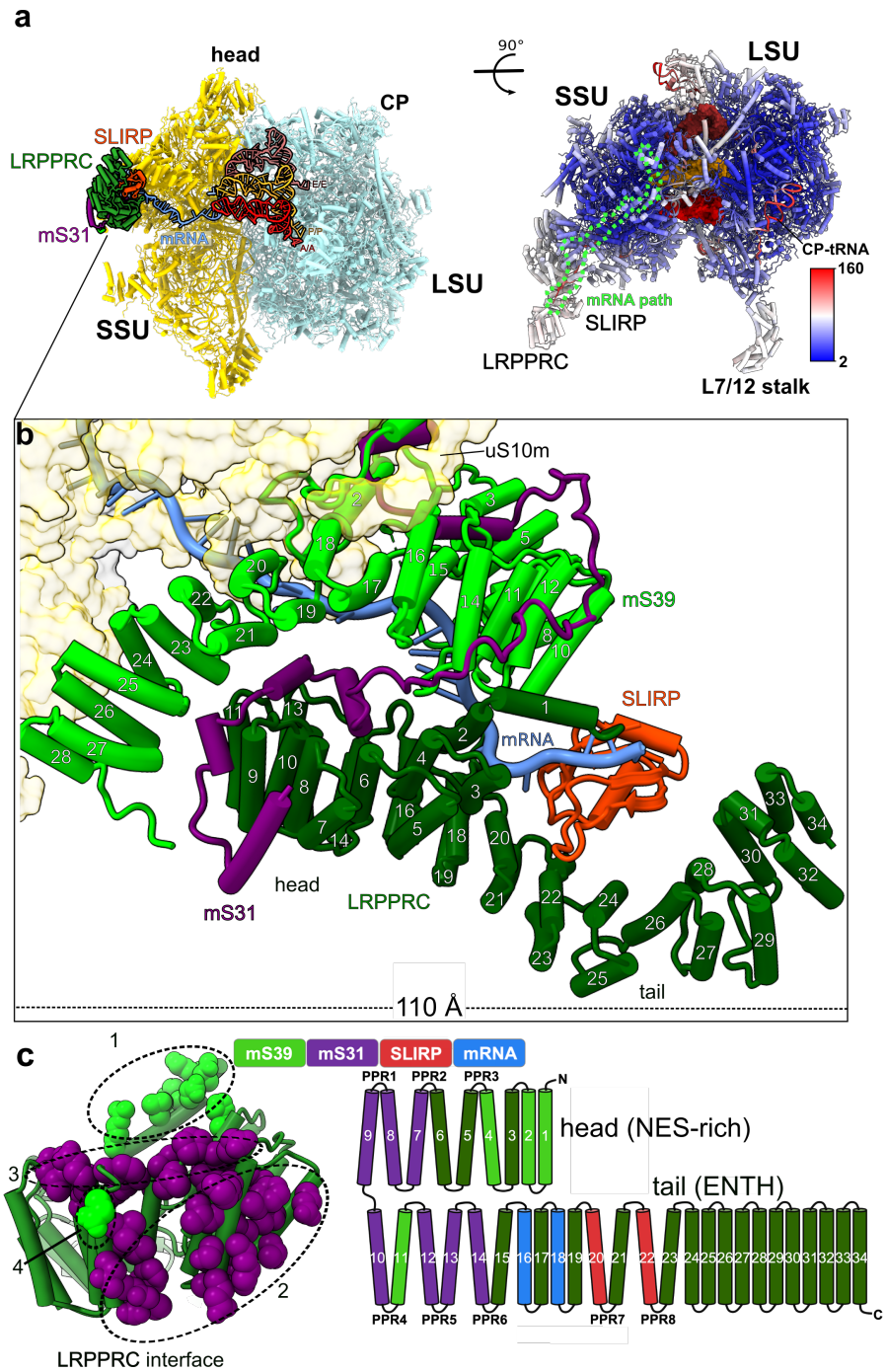

Fig. 1. Structure of mitoribosome with LRPPRC-SLIRP bound to mRNA.
a, Overview of the mitoribosome:LRPPRC-SLIRP model. Right panel, top view of the model colored by atomic *B*-factor (Å^2), tRNAs in surface, mRNA path (light green) is shown. **b,** A close-up view of the mitoribosome:LRPPRC-SLIRP-mRNA interactions. LRPPRC associates with mS31-39 via a superhelical ring-like structure (head) that together form a corridor for handing-off the mRNA from SLIRP. **c,** Contact sites between LRPPRC and mS31-mS39 (within 4 Å distance), view from the interface. Right panel, schematic diagram showing the topology of LRPPRC consisting of 34 helices arranged in head and tail domains. Colours represent engagement in interactions with mS39, mS31, SLIRP, mRNA.

118 To place the structural data into an evolutionary context, we performed comparative
119 phylogenetic analysis of the proteins involved in the mRNA handing-off process. Since the
120 mitochondrial rRNA has been generally reduced in metazoa[22], we examined whether this loss
121 might coincide with the origin of LRPPRC and its interactors. The orthology database
122 EGGNOGG[23] and previous analysis[24] indicated that LRPPRC and mS31 are only present in
123 Bilateria, while mS39 only occurs in metazoa. We then confirmed the results with more sensitive
124 detection[25] followed by manual sequence analysis examining domain composition, which put the
125 origin of LRPPRC and mS31 at the root of the metazoa. Thus, the appearance of the proteins
126 therewith coincides with the loss of parts of the rRNA (Fig. 2a). SLIRP appears to originate
127 slightly later than LRPPRC, but its small size makes determining its phylogenetic origin less
128 conclusive.
129 The correlation between rRNA reduction and protein acquisition is important, because the rRNA
130 regions H16 (410-432) and H33-37 (997-1118) that bridge the mRNA to the channel entrance in
131 bacteria[1] are either absent or reduced in the metazoan mitoribosome. However, a superposition
132 of the mitoribosome:LRPPRC-SLIRP-mRNA complex with *E. coli* expressome[1] shows not only
133 that the nascent mRNA follows a comparable path in both systems, but also the mRNA
134 delivering complexes bind in a similar location with respect to their ribosomes (Fig. 2b). To test
135 whether homolog protein interactions can explain the conservation, we compared the interfaces.
136 Indeed, in the NusG-coupled expressome, NusG binds to uS10 and restrains RNAP motions[1],
137 and in our structure uS10m has a related interface between helix α2 with mS31-mS39, which
138 induces association of these two proteins (Fig. 2c, Extended Data Fig. 3). Yet, most of the
139 interactions rely on a mito-specific N-terminal extension of uS10m engaging in a shared sheet
140 with mS39 via strand β1, and helices α1,16 and 18 are further involved in the binding (Extended
141 Data Fig. 3). Together, this suggests that a specific protein-based mechanisms must have evolved
142 in the evolution of the metazoan mitoribosome for mRNA recognition and protection.
143 Overall, these findings redefine the mitoribosome-LRPPRC-SLIRP as the central regulator of
144 mitochondrial gene expression and explain how the newly identified components modulate the
145 function of translation via mRNA binding. This represents a step that follows a progression of
146 the SSU through the assembly pathway[26] and preinitiation[27] that have been previously
147 determined. Since the presence of large RNA-binding moieties was also reported in association
148 with mitoribosomes in other species[28-32], the regulation principle of transcription-translation with
149 mitochondrial molecular connects might be a general feature.
150

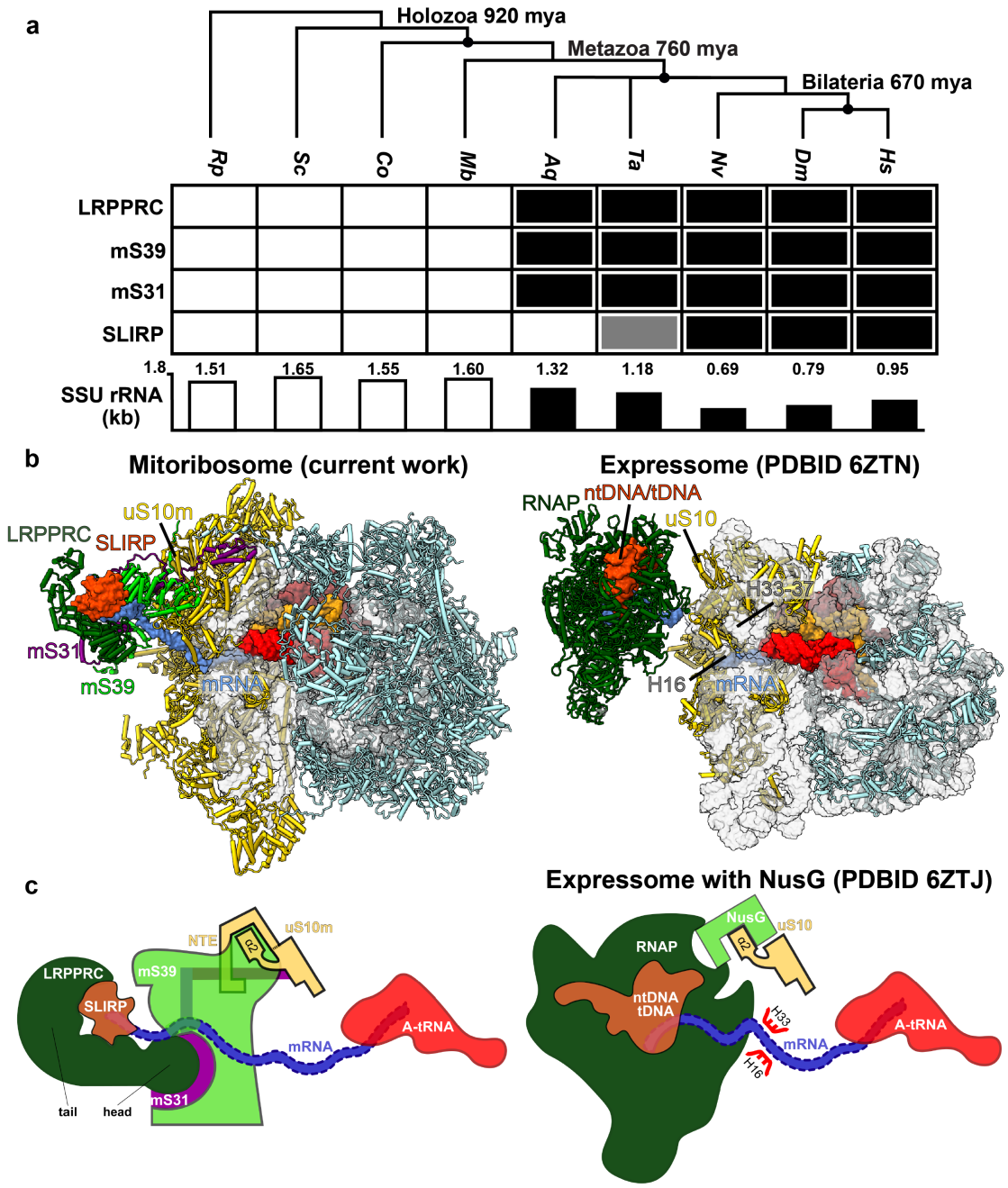

Fig 2. Formation of mitoribosome:LRPPRC-SLIRP and 70S-RNAP complexes. **a,** Phylogenetic analysis shows correlation between acquisition of LRPPRC, SLIRP, mS31, mS39 and reduction of rRNA in metazoa. Black rectangles indicate the presence of proteins, grey indicates uncertainty about the presence of an ortholog. *Hs*: *Homo sapiens, Ds: Drosophila melanogaster, Nv*: *Nematostella vectensis, Ta: Trichoplax adhaerens, Aq*: *Amphimedon queenslandica* (sponge)*, Mb*: *Monosiga brevicollis* (unicellular choanoflagellate)*, Co*: *Capsaspora owczarzaki* (protist)*, Sc*: *Saccharomyces cerevisiae* (fungi)*, Rp*: *Rickettsia prowazekii* (alpha-proteobacterium). Dating in million years ago (myo) is based on ref 33. **b,** Model of the mitoribosome:LRPPRC-SLIRP complex compared with uncoupled model of the expressome from *E.coli*[3]. **c,** Schematic representation indicating a more stable association of mRNA-delivering proteins in the mitoribosome compared to NusG-coupled expressome[1].

References

1. Webster, M. W. *et al.* Structural basis of transcription-translation coupling and collision in bacteria. *Science* **369,** 1355–1359 (2020).
2. Wang, C. *et al.* Structural basis of transcription-translation coupling. *Science* **369,** 1359–1365 (2020).
3. O'Reilly, F. J. *et al.* In-cell architecture of an actively transcribing-translating expressome. *Science* **369,** 554–557 (2020).
4. Itoh, Y. *et al.* Mechanism of membrane-tethered mitochondrial protein synthesis. *Science* **371,** 846–849 (2021).
5. Ott, M., Amunts, A. & Brown, A. Organization and regulation of mitochondrial protein synthesis. *Annual Review of Biochemistry* **85,** 77–101 (2016).
6. Ruzzenente, B. *et al.* LRPPRC is necessary for polyadenylation and coordination of translation of mitochondrial mrnas. *The EMBO Journal* **31,** 443–456 (2011).
7. Siira, S. J. *et al.* LRPPRC-mediated folding of the mitochondrial transcriptome. *Nature Communications* **8,** (2017).
8. Chujo, T. *et al.* LRPPRC/SLIRP suppresses pnpase-mediated mrna decay and promotes polyadenylation in human mitochondria. *Nucleic Acids Research* **40,** 8033–8047 (2012).
9. Sasarman, F., Brunel-Guitton, C., Antonicka, H., Wai, T. & Shoubridge, E. A. LRPPRC and SLIRP interact in a ribonucleoprotein complex that regulates posttranscriptional gene expression in mitochondria. *Molecular Biology of the Cell* **21,** 1315–1323 (2010).
10. Mootha, V. K. *et al.* Identification of a gene causing human cytochrome *c* oxidase deficiency by Integrative Genomics. *Proceedings of the National Academy of Sciences* **100,** 605–610 (2003).
11. Aibara, S., Singh, V., Modelska, A. & Amunts, A. Structural basis of mitochondrial translation. *eLife* **9,** (2020).
12. Soto, I. *et al.* Balanced mitochondrial and cytosolic translatomes underlie the biogenesis of human respiratory complexes. (2021). doi:10.1101/2021.05.31.446345
13. Lagouge, M. *et al.* SLIRP regulates the rate of mitochondrial protein synthesis and protects LRPPRC from degradation. *PLOS Genetics* **11,** (2015).
14. Baughman, J. M. *et al.* A computational screen for regulators of oxidative phosphorylation implicates SLIRP in mitochondrial RNA homeostasis. *PLoS Genetics* **5,** (2009).
15. Guo, L. *et al.* Pathogenic SLIRP variants as a novel cause of autosomal recessive mitochondrial encephalomyopathy with complex I and IV deficiency. *European Journal of Human Genetics* **29,** 1789–1795 (2021).
16. Sasarman, F. *et al.* Tissue-specific responses to the LRPPRC founder mutation in French Canadian leigh syndrome. *Human Molecular Genetics* **24,** 480–491 (2014).

17. Xu, F., Addis, J. B. L., Cameron, J. M. & Robinson, B. H. LRPPRC mutation suppresses cytochrome oxidase activity by altering mitochondrial RNA transcript stability in a mouse model. *Biochemical Journal* **441,** 275–283 (2011).
18. Amunts, A., Brown, A., Toots, J., Scheres, S. H. & Ramakrishnan, V. The structure of the human mitochondrial ribosome. *Science* **348,** 95–98 (2015).
19. Greber, B. J. *et al.* The complete structure of the 55 *s* mammalian mitochondrial ribosome. *Science* **348,** 303–308 (2015).
20. Spåhr, H. *et al.* SLIRP stabilizes LRPPRC via an RRM–PPR protein interface. *Nucleic Acids Research* **44,** 6868–6882 (2016).
21. Coquille, S. & Thore, S. Leigh syndrome-inducing mutations affect LRPPRC / SLIRP complex formation. (2020). doi:10.1101/2020.04.16.044412
22. Petrov, A. S. *et al.* Structural patching fosters divergence of mitochondrial ribosomes. *Molecular Biology and Evolution* **36,** 207–219 (2018).
23. Huerta-Cepas, J. *et al.* Eggnog 5.0: A hierarchical, functionally and phylogenetically annotated orthology resource based on 5090 organisms and 2502 viruses. *Nucleic Acids Research* **47,** (2018).
24. Sterky, F. H., Ruzzenente, B., Gustafsson, C. M., Samuelsson, T. & Larsson, N.-G. LRPPRC is a mitochondrial matrix protein that is conserved in metazoans. *Biochemical and Biophysical Research Communications* **398,** 759–764 (2010).
25. Eddy, S. R. Accelerated profile HMM searches. *PLoS Computational Biology* **7,** (2011).
26. Khawaja, A. *et al.* Distinct pre-initiation steps in human mitochondrial translation. *Nat Commun* **11**, 2932, doi:10.1038/s41467-020-16503-2 (2020).
27. Itoh, Y. *et al.* Mechanism of mitoribosomal small subunit biogenesis and preinitiation. *Nature* **606,** 603–608 (2022).
28. Amunts, A. *et al.* Structure of the yeast mitochondrial large ribosomal subunit. *Science* **343,** 1485–1489 (2014).
29. Tobiasson, V. & Amunts, A. Ciliate mitoribosome illuminates evolutionary steps of mitochondrial translation. *eLife* **9,** (2020).
30. Waltz, F., Soufari, H., Bochler, A., Giegé, P. & Hashem, Y. Cryo-EM structure of the RNA-rich plant mitochondrial ribosome. *Nature Plants* **6,** 377–383 (2020).
31. Waltz, F. *et al.* How to build a ribosome from RNA fragments in Chlamydomonas mitochondria. *Nature Communications* **12,** (2021).
32. Tobiasson, V., Berzina, I. & Amunts, A. Structure of a mitochondrial ribosome with fragmented rRNA in complex with membrane-targeting elements. *Nature Communications* (in revision).
33. Erwin, D. H. Early metazoan life: Divergence, environment and ecology. *Philosophical Transactions of the Royal Society B: Biological Sciences* **370,** 20150036 (2015).

238 **Methods**

239 Experimental model and culturing

240 HEK293S-derived cells (T501) were grown in Freestyle 293 Expression Medium containing 5%
241 tetracycline-free fetal bovine serum (FBS) in vented shaking flasks at 37°C, 5% CO_2 and 120
242 rpm (550 x g). Culture was scaled up sequentially, by inoculating at 1.5 x 10^6 cells/mL and
243 subsequently splitting at a cell density of 3.0 x 10^6 cells/mL. Finally, a final volume of 2 L of cell
244 culture at a cell density of 4.5 x 10^6 cells/mL was used for mitochondria isolation, as previously
245 described[34].

246

247 Mitoribosome purification

248 HEK293S-derived cells were harvested from the 2 L culture when the cell density was 4.2 x 10^6
249 cells/mL by centrifugation at 1,000 g for 7 min, 4 °C. The pellet was washed and resuspended in
250 200 mL Phosphate Buffered Saline (PBS). The washed cells were pelleted at 1,000 g for 10 min
251 at 4 °C. The resulting pellet was resuspended in 120 mL of MIB buffer (50 mM HEPES-KOH,
252 pH 7.5, 10 mM KCl, 1.5 mM $MgCl_2$, 1 mM EDTA, 1 mM EGTA, 1 mM dithiothreitol,
253 cOmplete EDTA-free protease inhibitor cocktail (Roche), and allowed to swell in the buffer for
254 15 min in the cold room by gentle stirring. About 45 mL of SM4 buffer (840 mM mannitol, 280
255 mM sucrose, 50 mM HEPES-KOH, pH 7.5, 10 mM KCl, 1.5 mM $MgCl_2$, 1 mM EDTA, 1 mM
256 EGTA, 1 mM DTT, 1X cOmplete EDTA-free protease inhibitor cocktail (Roche) was added to
257 the cells in being stirred in MIB buffer and poured into a nitrogen cavitation device kept on ice.
258 The cells were subjected to a pressure of 500 psi for 20 min before releasing the nitrogen from
259 the chamber and collecting the lysate. The lysate was clarified by centrifugation at 800 x g and 4
260 °C, for 15 min, to separate the cell debris and nuclei. The supernatant was passed through a
261 cheesecloth into a beaker kept on ice. The pellet was resuspended in half the previous volume of
262 MIBSM buffer (3 volumes MIB buffer + 1 volume SM4 buffer) and homogenized with a
263 Teflon/glass Dounce homogenizer. After clarification as described before, the resulting lysate
264 was pooled with the previous batch of the lysate and subjected to centrifugation at 1,000 x g, 4
265 °C for 15 minutes to ensure complete removal of cell debris. The clarified and filtered
266 supernatant was centrifuged at 10,000 x g and 4 °C for 15 min to pellet crude mitochondria.
267 Crude mitochondria were resuspended in 10 mL MIBSM buffer and treated with 200 units of
268 Rnase-free Dnase (Sigma-Aldrich) for 20 min in the cold room to remove contaminating
269 genomic DNA. Crude mitochondria were again recovered by centrifugation at 10,000 g, 4 °C for
270 15 min and gently resuspended in 2 mL SEM buffer (250 mM sucrose, 20 mM HEPES-KOH,
271 pH 7.5, 1 mM EDTA). Resuspended mitochondria were subjected to a sucrose density step-
272 gradient (1.5 mL of 60% sucrose; 4 mL of 32% sucrose; 1.5 mL of 23% sucrose and 1.5 mL of
273 15% sucrose in 20 mM HEPES-KOH, pH 7.5, 1 mM EDTA) centrifugation in a Beckmann
274 Coulter SW40 rotor at 28,000 rpm (139,000 x g) for 60 min. Mitochondria seen as a brown band
275 at the interface of 32% and 60% sucrose layers were collected and snap-frozen using liquid
276 nitrogen and transferred to −80 °C.

277 Frozen mitochondria were transferred on ice and allowed to thaw slowly. Lysis buffer (25 mM
278 HEPES-KOH, pH 7.5, 50 mM KCl, 10 mM $Mg(Oac)_2$, 2% polyethylene glycol octylphenyl
279 ether, 2 mM DTT, 1 mg/mL EDTA-free protease inhibitors (Sigma-Aldrich) was added to
280 mitochondria and the tube was inverted several times to ensure mixing. A small Teflon/glass
281 Dounce homogenizer was used to homogenize mitochondria for efficient lysis. After incubation
282 on ice for 5-10 min, the lysate was clarified by centrifugation at 30,000 x g for 20 min, 4 °C. The
283 clarified lysate was carefully collected. Centrifugation was repeated to ensure complete
284 clarification. A volume of 1 mL of the mitochondrial lysate was applied on top of 0.4 mL of 1 M
285 sucrose (v/v ratio of 2.5:1) in thick-walled TLS55 tubes. Centrifugation was carried out at
286 231,500 x g for 45 min in a TLA120.2 rotor at 4 °C. The pellets thus obtained were washed and
287 sequentially resuspended in a total volume of 100 µl resuspension buffer (20 mM HEPES-KOH,
288 pH 7.5, 50 mM KCl, 10 mM $Mg(Oac)_2$, 1% Triton X-100, 2 mM DTT). The sample was
289 clarified twice by centrifugation at 18,000 g for 10 min at 4 °C. The sample was applied on to a
290 linear 15-30% sucrose (20 mM HEPES-KOH, pH 7.5, 50 mM KCl, 10 mM $Mg(Oac)_2$, 0.05% n-
291 dodecyl-β-D-maltopyranoside, 2 mM DTT) gradient and centrifuged in a TLS55 rotor at 213,600
292 x g for 120 min at 4 °C. The gradient was fractionated into 50 µL volume aliquots. The
293 absorption for each aliquot at 260 nm was measured and fractions corresponding to the
294 monosome peak were collected. The pooled fractions were subjected to buffer exchange with the
295 resuspension buffer.

296

297 Cryo-EM data acquisition

298 3 µL of ~120 nM mitoribosome was applied onto a glow-discharged (20 mA for 30 sec) holey-
299 carbon grid (Quantifoil R2/2, copper, mesh 300) coated with continuous carbon (of ~3 nm
300 thickness) and incubated for 30 sec in a controlled environment of 100% humidity and 4 ºC. The
301 grids were blotted for 3 sec, followed by plunge-freezing in liquid ethane, using a Vitrobot
302 MKIV (FEI/Thermofischer). The data were collected on FEI Titan Krios (FEI/Thermofischer)
303 transmission electron microscope operated at 300 keV, using C2 aperture of 70 µm and a slit
304 width of 20 eV on a GIF quantum energy filter (Gatan). A K2 Summit detector (Gatan) was used
305 at a pixel size of 0.83 Å (magnification of 165,000X) with a dose of 29-32 electrons/$Å^2$
306 fractionated over 20 frames.

307

308 Cryo-EM data processing

309 The beam-induced motion correction and per-frame B-factor weighting were performed using
310 RELION-3.0.2[35,36]. Motion-corrected micrographs were used for contrast transfer function (CTF)
311 estimation with gctf[37]. Unusable micrographs were removed by manual inspection of the
312 micrographs and their respective calculated CTF parameters. Particles were picked in RELION-
313 3.0.2 , using reference-free followed by reference-aided particle picking procedures. Reference-
314 free 2D classification was carried out to sort useful particles from falsely picked objects, which
315 were then subjected to 3D classification. 3D classes corresponding to unaligned particles and

316 LSU were discarded and monosome particles were pooled and used for 3D auto-refinement
317 yielding a map with an overall resolution of 2.9-3.4 Å for the five datasets. Resolution was
318 estimated using a Fourier Shell Correlation cut-off of 0.143 between the two reconstructed half
319 maps. Finally, the selected particles were subjected to per-particle defocus estimation, beam-tilt
320 correction and per-particle astigmatism correction followed by Bayesian polishing. Bayesian
321 polished particles were subjected to a second round per-particle defocus correction. A total of
322 994,919 particles were pooled and separated into 86 optics groups in RELION-3.1[38], based on
323 acquisition areas and date of data collection. Beam-tilt, magnification anisotropy and higher-
324 order (trefoil and fourth-order) aberrations were corrected in RELION-3.1[38]. Particles with A-
325 site and/or P-site occupied with tRNAs which showed comparatively higher occupancy for the
326 unmodeled density potentially corresponding to LRPPRC-SLIRP module were pooled and re-
327 extracted in a larger box size of 640 Å. The re-extracted particles were subjected to 3D
328 autorefinement in RELION3.1[38]. This was followed by sequential signal subtraction to remove
329 signal from the LSU, and all of the SSU except the region around mS39 and the unmodeled
330 density, in that order. This was followed by masked 3D classification (T=200) to enrich for
331 particles carrying the unmodeled density. Using a binary mask covering mS39 and all of the
332 unmodeled density, we performed local-masked refinement on resulting 41,812 particles within
333 an extracted sub-volume of 240 Å box size leading to 3.37 Å resolution map.

334

335 Model building and refinement

336 At the mRNA channel entrance, a more accurate and complete model of mS39 could be built
337 with 29 residues added to the structure. Improved local resolution enabled unambiguous
338 assignment of residues to the density which allowed us to address errors in the previous model.
339 A total of 28 α-helices could be modeled in their correct register and orientation. Further, a 28-
340 residue long N-terminal loop of mS31 (residues 247–275) along mS39 and mito-specific N-
341 terminal extension of uS9m (residues 53–70) approaching mRNA were modeled by fitting the
342 loops in to the density maps.

343 For building LRPPRC-SLIRP module, the initial model of the full length LRPPRC was obtained
344 from *AlphaFold2*[39] Protein Structure Database (Uniprot ID P42704). Based on the analysis, three
345 stable domains were identified that are connected by flexible linkers (673-983, 1035-1390). We
346 then systematically assessed the domains against the map, and the N-terminal region (77-660)
347 could be fitted into the density. The initial model was real space refined into the 3.37 Å
348 resolution map of mS39-LRPPRC-SLIRP region obtained after partial signal subtraction using
349 reference-restraints in *Coot* v0.9[40]. The N-terminal region covering residues 64-76 was identified
350 in the density map and allowed us to model 34 helices of LRPPRC (residues 64-644). Helices
351 α1-29 could be confidently modeled. An additional five helices, as predicted by *Alphafold2*[39],
352 could be accommodated into the remaining density. After modelling LRPPRC into the map,
353 there was an unaccounted density that fits SLIRP. The initial model of SLIRP was obtained from
354 *Alphafold2*[39] Protein Structure Database (Uniprot ID Q9GZT3). The unmodeled density agreed

with the secondary structure of SLIRP. The model was real space refined into the density using reference-restraints as was done for LRPPRC in *Coot* v0.9[40]. Five additional RNA residues could be added to the 3' terminal of mRNA to account for tubular density extending from it along the mRNA binding platform. The A/A P/P E/E state model was rigid body fitted into the corresponding 2.85 Å resolution consensus map. Modeled LRPPRC was merged with the rigid body fitted monosome model to obtain a single model of the mitoribosome bound to LRPPRC and SLIRP. The model was then refined against the composite map using PHENIX v1.18[41] (Supplementary Information Table 1).

Phylogenetic analysis

Phylogenetic distribution of proteins was determined by examining phylogeny databases[42], followed by sensitive homology detection to detect homologs outside of the bilateria. Orthologs were required to have identical domain compositions, and Dollo parsimony was used to infer the evolutionary origin of a protein from its phylogenetic distribution. When multiple homologs of a protein were detected in a species, a neighbor-joining phylogeny was constructed to asses monophyly of putative orthologs to the human protein. The short length of the SLIRP candidate protein from *T. adhaerens* (B3SAC0_TRIAD), that is part of the large RRM family, precludes obtaining a reliable phylogeny to confidently assess orthology and its orthology to human SLIRP is therefore tentative.

Data availability statement

The atomic coordinates were deposited in the RCSB Protein Data Bank, and EM maps have been deposited in the Electron Microscopy Data bank under accession numbers: XXXX and EMD-XXXXX.

The atomic coordinates that were used in this study: 6ZTJ (*E.coli* 70S-RNAP expressome complex in NusG); 6ZTN (*E.coli* 70S-RNAP expressome complex in NusG).

Additional References

34. Aibara, S., Andréll, J., Singh, V. & Amunts, A. Rapid isolation of the mitoribosome from Hek Cells. *Journal of Visualized Experiments* (2018). doi:10.3791/57877
35. Zivanov, J. *et al.* New tools for automated high-resolution cryo-EM structure determination in relion-3. *eLife* **7,** (2018).
36. Zivanov, J., Nakane, T. & Scheres, S. H. A bayesian approach to beam-induced motion correction in Cryo-EM single-particle analysis. *IUCrJ* **6,** 5–17 (2019).
37. Zhang, K. GCTF: Real-time CTF determination and correction. *Journal of Structural Biology* **193,** 1–12 (2016).

38. Zivanov, J., Nakane, T. & Scheres, S. H. Estimation of high-order aberrations and anisotropic magnification from Cryo-EM data sets in *relion*-3.1. *IUCrJ* **7,** 253–267 (2020).

39. Jumper, J. *et al.* Highly accurate protein structure prediction with alphafold. *Nature* **596,** 583–589 (2021).

40. Emsley, P. & Cowtan, K. *coot*: Model-building tools for Molecular Graphics. *Acta Crystallographica Section D Biological Crystallography* **60,** 2126–2132 (2004).

41. Afonine, P. V. *et al.* Real-space refinement in*phenix*for cryo-EM and Crystallography. *Acta Crystallographica Section D Structural Biology* **74,** 531–544 (2018).

42. Huerta-Cepas, J. *et al.* Eggnog 5.0: A hierarchical, functionally and phylogenetically annotated orthology resource based on 5090 organisms and 2502 viruses. *Nucleic Acids Research* **47,** (2018).

Acknowledgments

We thank S. Aibara and J. Andrell for help with data collection. The research was funded by the Swedish Foundation for Strategic Research (FFL15:0325), Ragnar Söderberg Foundation (M44/16), European Research Council (ERC-2018-StG-805230), Knut and Alice Wallenberg Foundation (2018.0080), V.S. was supported by the Horizon 2020 - Marie Sklodowska-Curie Innovative Training Network (721757). Y.I. was supported by H2020-MSCA-IF-2017 (799399-Itohribo). The SciLifeLab cryo-EM facility is funded by the Knut and Alice Wallenberg, Family Erling Persson, and Kempe foundations.

Author contributions

V.S. and Y.I. collected cryo-EM data, processed the data, and built the models. V.S., Y.I. and A.A. carried out structural analysis. V.S., M.H. and A.A. performed evolutionary analysis. A.A. wrote the manuscript. All authors contributed to data interpretation and manuscript writing.

Competing Interests Statement

The authors declare no competing interests.

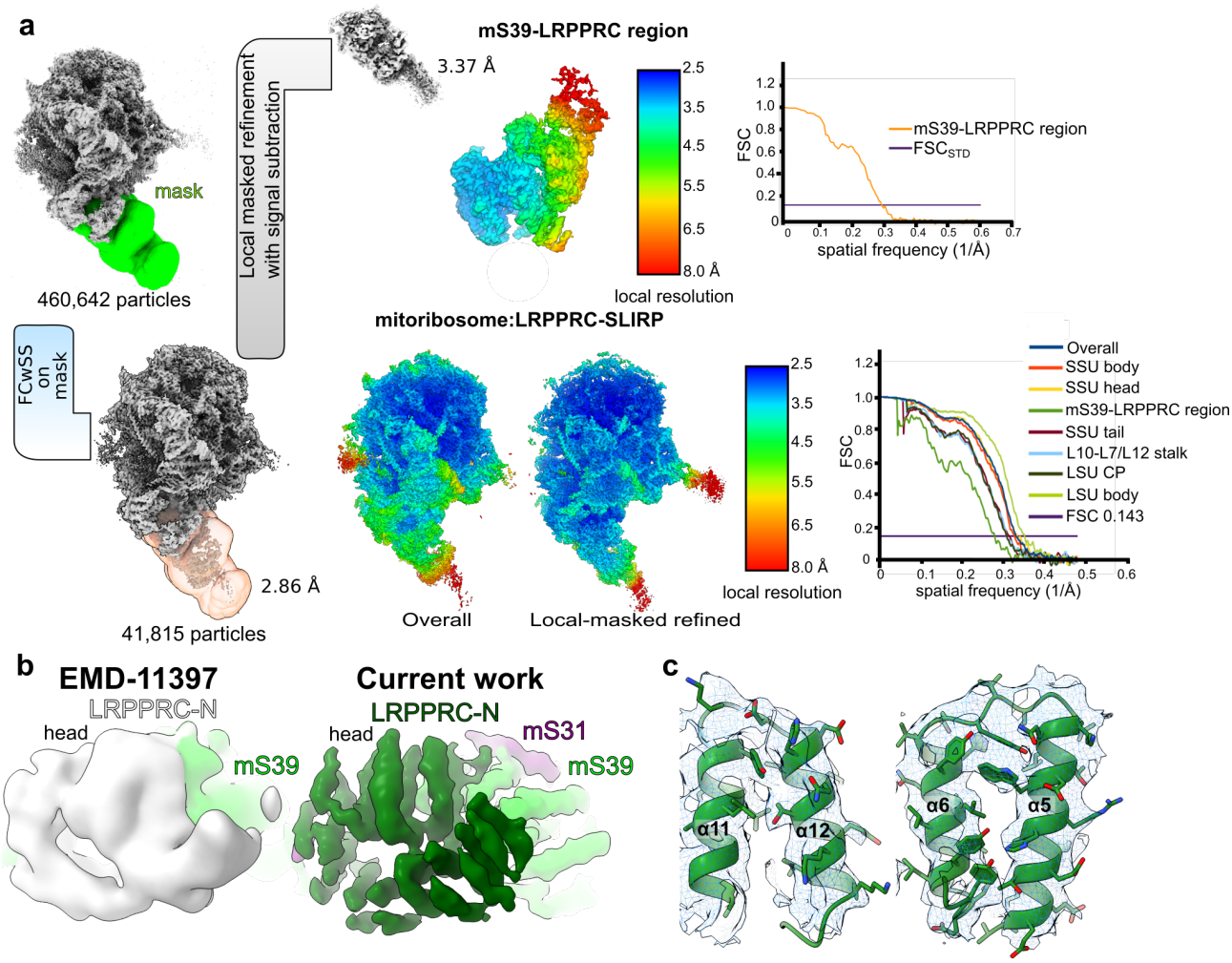

Extended Data fig. 1. Cryo-EM data processing and map for LRPPRC-SLIRP-mS39 region. **a.** Focused classification with signal subtraction around mS39-LRPPRC-SLIRP region on A/A- or P/P-RNA containing particles to improve LRPPRC-SLIRP occupancy, followed by, focused masked refinement on mS39-LRPPRC-SLIRP region with signal subtraction to improve local resolution (left). Fourier shell correlation curves for the overall and masked maps (right). Binary masks used for local-masked refinements. Local-masked refinements are shown and colored by local resolution (middle). **b.** Map comparison for LRPPRC region between our work and EMD-11397. Map has been Gaussian filtered for better visibility. **c.** Density map around helices α11-12 and 5-6.

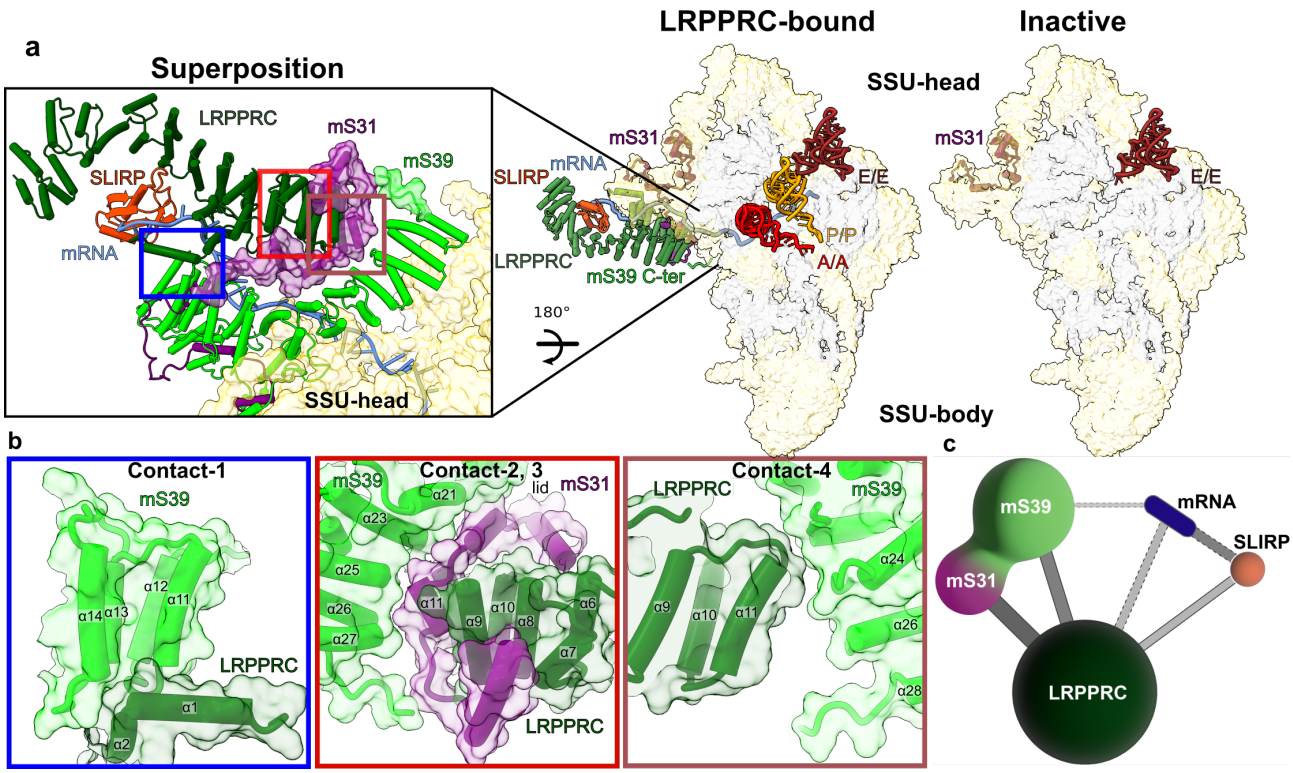

Extended Data fig. 2. LRPPRC-SLIRP contacts with SSU head and high resolution features identified in the structure. a. Comparison of SSU from mitoriboome:LRPPRC-SLIRP complex with SSU from E-site tRNA bound monosome. Zoom-in shows N-terminal region of mS31 and C-terminal loop of mS39 (in surface) stabilized by LRPPRC. **b.** Contact regions of LRPPRC with mS31 and mS39. **c.** Schematic depicting interface of LRPPRC with SLIRP, mS31, mS39 and mRNA. Size of circles corresponds to molecular weight of the protein.

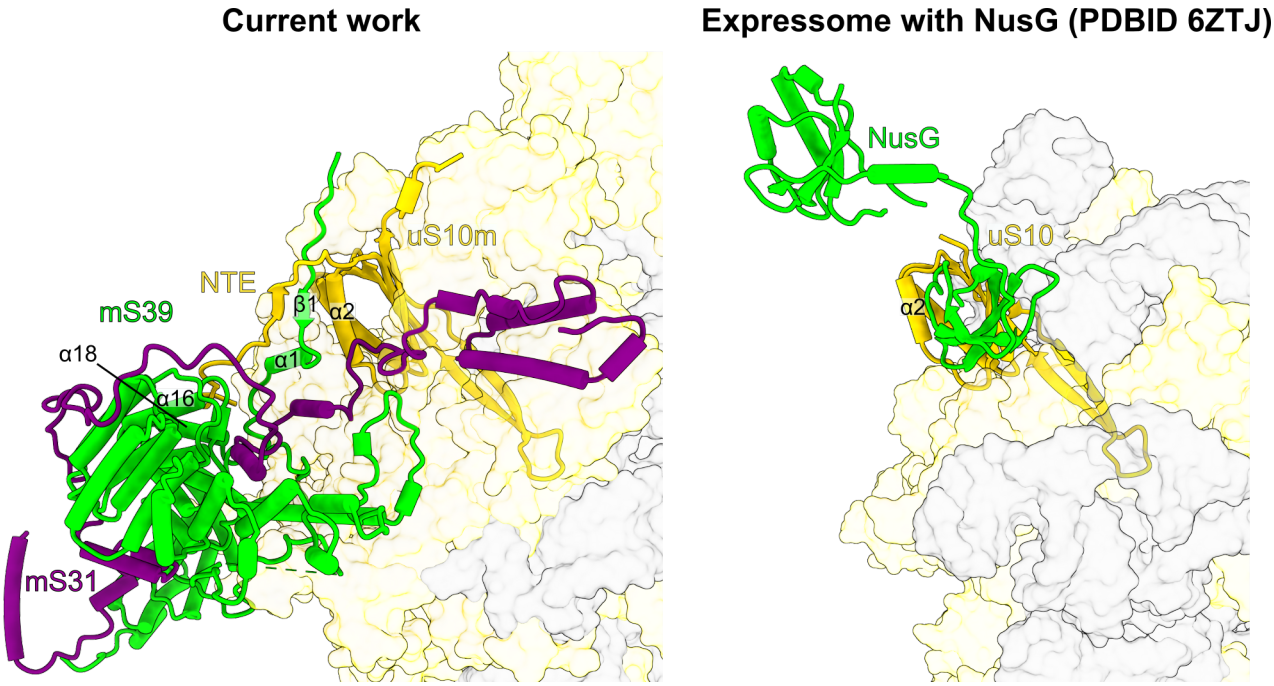

Extended Data fig. 3. Close-up view of uS10m interactions with mS31-mS39.
Interface between uS10m with mS31-mS39 that serve as the platform for LRPPRC-SLIRP is similar to that formed between uS10 and NusG that binds RNA polymerase in bacterial expressome[1].

Activation mechanism of mitochondrial translation by LRPPRC-SLIRP

Vivek Singh[1], Yuzuru Itoh[1], Martijn A Huynen[2], Alexey Amunts[1*]

[1] Science for Life Laboratory, Department of Biochemistry and Biophysics, Stockholm University, 17165 Solna, Sweden.
[2] Department of Molecular and Cellular Pharmacology, University of Miami Miller School of Medicine, Miami, FL 33136, United States.

* correspondence: amunts@scilifelab.se

SUPPLEMENTARY INFORMATION

Table of contents:

Supplementary Table 1. Data collection and model statistics

SI Video 1. Structure of LRPPRC-SLIRP module bound to monosome

Supplementary table 1. Data collection and model statistics.

	Monosome with LRPPRC:SLIRP PDB: xxxx EMD-xxxxx
Data collection and processing	
Electron microscope	Titan Krios
Camera	K2 Summit (counting mode)
Magnification	165,000
Voltage (kV)	300
Electron exposure ($e^-/Å^2$)	29-32
No. of frames	20
Defocus range (μm)	-0.6 to -2.8
Pixel size (Å)	0.83
Symmetry imposed	C_1
Final particle number (no.)	41,815
Map resolution (Å) (Overall/ LSU-body/ CP/ L10-L12-stalk/ L1-stalk/ SSU-body/ SSU-head/ mS39/ SSU-tail/ mS39-LRPPRC-SLIRP)	2.85/2.69/ 3.07/ 3.07/ −/ 2.89/ 2.84/−/ 3.02/3.37
FSC threshold	0.143
Map resolution range (Å)	2.5-8.0
Refinement	
Initial model used (PDB code)	6ZSG, 6RW4
Model resolution (Å)	2.7
Model to map CC (CC_{volume})	0.84
FSC threshold	0.5
Map-sharpening *B* factor ($Å^2$) (Overall/ LSU-body/ CP/ L10-L12-stalk/ L1-stalk/ SSU-body/ SSU-head/ mS39/	-33/ -28/ -58/ -49/−/ -39/ -39/−/-55/ -60
Model composition	
Non-hydrogen atoms	356138
Hydrogen atoms	160529
Protein chains	90
RNA chains	7
Protein residues (non-modified/ *N*-acetylAla/ *N*-acetylSer/ *N*-acetylThr O^1-methylisoAsp)	15631/3/1/1/1
RNA residues (non-modified/ mG/ mU/ m^1A/ m^2G/ψ /m^4C/ m^5C/ m^5U/ $m^6{}_2A$)	2822/2/ 1/ 2/ 1/ 2/ 1/ 1/ 1/ 2
Ligands (ATP/ GDP/ NAD/ 2Fe-2S/ spermine/ spermidine/ putrescine)	1/ 1/ 1/ 3 /1 /4/ 1
Ions (Zn^{2+}/ K^+/ Mg^{2+})	3/ 58/ 207
Waters	7,702
Mean atomic *B*-factor ($Å^2$)	
Protein	38.74
RNA	36.58
Ligand	20
Water	16.55
Validation	
Ramanchandran plot (%)	
Outliers	0.04
Allowed	1.84
Favored	98.12
Clash score	2.61
RMSD	
Bonds (Å)	0.002
Angles (°)	0.429
Rotamer outliers (%)	0.00
C_β outliers (%)	0.00
CaBLAM outliers (%)	0.89

Supplementary Video 1. Structure of LRPPRC-SLIRP module bound to monosome.

The video shows the structure of LRPPRC-SLIRP determined in this work and how docking of mRNA on SSU is achieved by LRPPRC-SLIRP together with mito-specific proteins mS31 and mS39.